Metals and Materials International (2024) 30:1527–1537
https://doi.org/10.1007/s12540-023-01597-2

Effect of Extrusion Temperature on the Microsturcture in a Bismuth Modified Magnesium Alloy

Tingting Guo[1] · Yulei Tai[2,3] · Lu Jiang[4] · Zhen Zhang[5] · Jun Wang[4]

Received: 12 October 2023 / Accepted: 30 November 2023 / Published online: 13 January 2024

Abstract
Dilute Mg–Bi alloy is a recently developed alloy system with good extrudability and ductility. However, there is a limited understanding of the influence of extrusion temperature on its microstructure when extruded at lower temperatures (≤ 300 °C), which restricts the further enhancement of its mechanical properties. In this work, we investigated the microstructure evolution at multiscale levels (micro-scale, nanoscale, and atomic scale) affected by different extrusion temperatures. The results show that particle-stimulated nucleation by the pre-existed Mg_3Bi_2 particle can significantly refine the grains (even down to a grain size of ~ 80 nm), and it is a dominant dynamic recrystallized mechanism, especially at 100 °C and 200 °C, though, with negligible influence on the final texture. In addition, dynamic precipitation with nano-sized precipitates (tens of nanometers) occurs in these temperatures, and they can provide the Zenner pinning effect to hinder grain growth. Most significantly, deformation-induced bismuth clusters (which can potentially be tailored to provide significant strengthening without deteriorating the ductility) were observed both in the matrix and at grain boundaries in all the extrusion temperatures. As the temperature increases, the size and the density of these clusters increases. Finally, an attempt at quantification of the strengthening contributions from the grain size, nanoparticles, clusters, and solid solution is provided, indicating the significant effect of extrusion temperature on varying these contributions.

Keywords Dilute magnesium alloys · Extrusion temperatures · Mechanical properties · Multiscale microstructures · Bismuth clusters

1 Introduction

There has been increasing demand for high-strength and low-cost magnesium alloys for automotive applications. Dilute magnesium alloys, incorporating low-temperature or severe plastic deformation, can obtain balanced strength and ductility [1–4]. To date, most of the work examines the effect of solute elements to elicit information regarding the role of individual elements on the microstructure and texture modification in dilute Mg–Bi alloys [5–12]. Some recent papers [5, 7, 13] have shown that the addition of a small amount of Mn (~ 1–2 wt%) in Mg–Bi was an effective grain refiner via Zenner pinning effect [14] by dynamic precipitated nanoscale α-Mn particles during hot extrusion, and which can also provide Orowan hardening. Micro-alloying addition with Zn to Mg–Bi enhanced the age hardening responses [15, 16]. This enhancement was attributed to the fact that the rod-shaped Mg_2Zn served as the nucleation sites leading to finer and a high number density dispersed Mg_3Bi_2 prismatic plates. Zn was also observed to co-segregate with bismuth

Tingting Guo and Yulei Tai contributed equally to this work.

✉ Jun Wang
jun.wang2@deakin.edu.au

1 Faculty of Mechanical and Electrical Engineering, Kunming University of Science and Technology, Kunming 650504, China

2 School Laboratory of Medicine, Hangzhou Medical College, Hangzhou 310053, China

3 Key Laboratory of Biomarkers and In Vitro Diagnosis Translation of Zhejiang Province, Hangzhou 310063, China

4 Institute for Frontier Materials, Deakin University, Geelong, VIC 3216, Australia

5 Intelligent Manufacturing Institute, Hefei University of Technology, Hefei 230009, China

along the grain boundaries [5] in such a way that preferential grains growth with basal texture was restricted in short term annealing. When combined with Mn and other micro-elements, this addition can result in a substantial increase in yielding stress, achieving 378 MPa and a reasonable elongation of 16.8% (Mg–1Bi–1Mn–0.3Zn–1Al–0.5Ca (wt%)) [5]. Minor addition of Ca to Mg–1wt%Bi alloys, similar to the effect of rare-earth element in other magnesium alloys [17–19], generates $<2\ \overline{11}\ 2>$ texture after hot extrusion [11, 20]. Furthermore, Ca traces can enhance the dynamic recrystallization rates with fine grains sizes, yielding a good combination of yielding strength and elongation (see Mg–1Bi–1Zn–0.6Ca (wt%) in Ref. [12]).

Nonetheless, there is very little information in the present literature about systematically investigating the microstructure features at different scales (grains at the micro-scale, the second phase at the micro or nanoscale, and solute atoms at the atomic scale) in extruded dilute binary Mg–Bi alloys at low extrusion temperature (≤ 300 ℃) to reveal the influence of extrusion temperature, which is critical for the further enhancement of their mechanical properties.

One of the challenges associated with Mg–Bi alloys is that the constituent Mg_3Bi_2 particles are easily formed in casting and hard to dissolve in the heat treatment due to the high melting point (873 °C), which is usually detrimental to fracture toughness [21, 22]. However, coarse Mg_3Bi_2 particles can affect dynamic recrystallization via particle stimulated nucleation (PSN) [23] and hence refine the grain size [21, 24] or modify the deformation texture [25]. Low temperature extruded Mg–2.5 wt%Bi alloys studied by Somekawa and Singh [26] exhibited an ultrafine grain size of ~ 1.2 µm, and micron-sized Mg_3Bi_2 particles of a volume fraction of ~ 2.5% were also observed in their work. Because the course Mg_3Bi_2 particles can potentially have a significant effect on the grain refinement and texture, making an assessment of the role of Mg_3Bi_2 particles on recrystallization during extrusion is important.

Another potentially essential factor to consider in developing high-performance dilute magnesium alloys is the effect of solute atom clusters. They are known to enhance the strength of magnesium with little cost to ductility [27, 28], and are also known to change the type or dispersion of precipitates [29, 30]. Sasaki et al. [31]. recently found that a high number density of Al atoms was attracted to the vacancy clusters in a severely deformed (equal channel angular extrusion at 150 ℃) Mg–9 wt% Al alloy. Notably, the number density of Al clusters is comparable to the values in some aged-hardened aluminum alloys. This result does show that it is feasible to produce dense deformation-induced solute clusters, and they are highly possible to empower magnesium alloys with a substantial strengthening response. First-principle calculation suggested that bismuth in magnesium displays negative grain boundary segregation energy and negative cohesive energy [32, 33]. This result indicates that bismuth atoms prefer not only to segregate at grain boundaries but also to form clusters. Hence, solute cluster hardening is possible in the Mg–Bi alloy system.

Therefore, in this work, we investigated the microstructure evolution at multiscale levels (micro-scale, nanoscale, and atomic scale) and to reveal the influence of extrusion temperature (100 ℃, 200 ℃, and 300 ℃) on a dilute Mg–2 wt% Bi alloy. Pure magnesium samples extruded at the same conditions were also prepared for comparison.

2 Experimental Details

The as-received Mg–2 wt% Bi cast ingot was homogenized at 480 °C for 6 h. This was followed by the extrusion at 100 °C, 200 °C, and 300 °C, respectively, with an extrusion ratio of 18 and a ram speed of 1.7 mm/s. Extrudates were quenched in the water immediately to inhibit the grain growth. Pure Magnesium extrusion samples were prepared with the same processing. Dog-bone-shaped samples with a gauge dimension of $\phi 3$ mm × 10 mm for tensile testing were prepared and tested at a strain rate of 10^{-3} s^{-1} at room temperature. The contact extensometer (Epsilon, produced by Epsilon Technology Corp, USA) is employed for strain measurement until fracture.

The microstructures of the longitudinal section of the extrudates along the extrusion axis were examined. Electron backscattered diffraction (EBSD) was employed by a field emission Zeiss Sigma 500 Scanning Electron Microscope (SEM) to obtain the initial crystallographic texture. The zone of interest was extracted by Focused Ion Beam (FIB) in Thermo Scientific Scios 2 and deposited to a copper grid for inspection by an FEI Tekna G^2 F30 transmission electron microscope (TEM) for characterizing the features of the nano particles and the grain size. A double aberration-corrected Thermo Fisher Scientific Themis Z scanning transmission electron microscope was utilized for atomic-scale imaging.

Atom probe tomography (APT) samples were prepared by the standard two-step electropolishing. APT were performed on a CAMECA Local Electrode Atom Probe LEAP 5000XR instrument, at 40 K with a pulse fraction of 20%, and a detection rate of 0.5%. Because bismuth has a very high atomic weight, a pulse repetition rate of 50 kHz was selected. APT data were reconstructed and analyzed with the IVAS embedded in CAMECA AP suite 6 software.

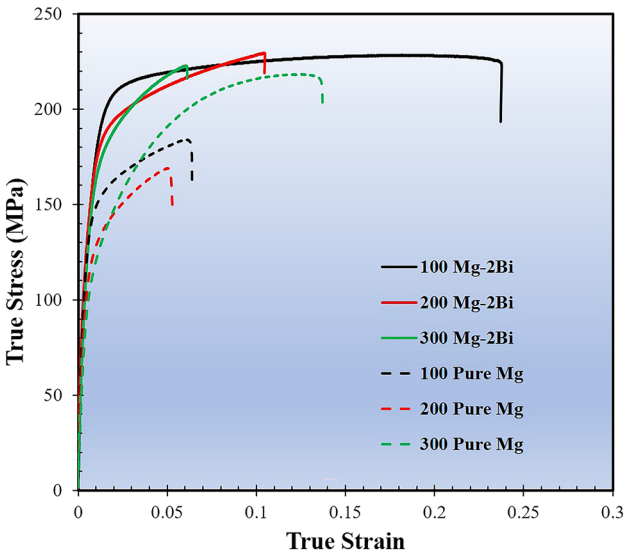

Fig. 1 Tensile true stress-true strain curves of Mg–2Bi and Pure magnesium extruded at 100 °C, 200 °C and 300 °C, respectively. With increasing extrusion temperatures, the 0.2% offset yielding stress of Mg–2Bi is 187 ± 8 MPa, 180 ± 2 MPa, and 167 ± 4 MPa, respectively, and the 0.2% proof stress of pure magnesium is 146 ± 8 MPa, 122 ± 5 MPa, and 107 ± 7 MPa, respectively

3 Results and Discussion

3.1 Mechanical Response

The representative true stress-true strain curves of tensile testing for Mg–2Bi and pure magnesium performed at different temperatures are presented in Fig. 1. It is seen that the yielding strength for both Mg–2Bi and pure magnesium decreases with increasing the extrusion temperature, which is the general rule for most magnesium extrudates [34]. Alloying with bismuth obviously strengthens the magnesium at different levels for all the cases. Compared to pure Mg, the average 0.2% proof strength increases by ~ 41 MPa, ~ 58 MPa, and ~ 60 MPa with increased extrusion temperature, respectively. The Mg–2Bi extruded at 100 °C exhibits the best mechanical property with a ductility of ~ 25%, and the value markedly dropped to lower than ~ 15% at higher extrusion temperatures. The situation for pure magnesium is different, i.e., it shows a brittle feature (the elongation is close to ~ 5%) at two lower extrusion temperatures while the elongation is enhanced to ~ 13% when samples were extruded at 300 °C.

3.2 Grains and Texture

To help interpret the temperature influence on the improved mechanical properties of Mg–2Bi alloy, Fig. 2 shows the microstructures taken by EBSD and the corresponding inverse pole figure (IPF) for each condition. Micro-alloying with bismuth could effectively promote dynamic recrystallization efficiency and refine grains. This effect is more significant for specimens extruded at 100 °C. The fully recrystallized grains were refined to a sub-micron size of ~ 1.2 μm, the same as that reported by Somekawa et al. via a similar extrusion process [26]. Pure magnesium at the same extrusion temperature, on the other hand, contains ~ 50% (area fraction) un-recrystallized (unDRXed) grains, which should be partially responsible for the dropped yielding strength and the ductility compared to its Mg–2Bi counterpart. At the temperature of 200 °C, a small amount of unDRXed grains is observed in both Mg–2Bi and pure Mg. The heterogeneity of the grain structure leads to the deterioration of the ductility compared to those extruded at 100 °C. When extrusion temperature rises to 300 °C, an almost fully recrystallized bimodal grain structure in Mg–2Bi alloy is clearly observed, consisting of fine grains of several microns around the coarse particles and coarse grains with a diameter of ~ 20–50 μm (45% area fraction). The corresponding grain orientation spread (GOS) map in Fig. 2g suggests the internal strain energy in area of large grains is relatively smaller. The matrix around the coarse particles, on the other hand, exhibits the greater GOS, indicating that the presence of particles promotes local nucleation sites and accelerates the recrystallization. By contrast, pure magnesium shows a more uniform distributed and fully recrystallized grain structure, which promotes ductility.

The corresponding inverse pole figures for each case are shown in Fig. 2h. Most materials show a $<10\bar{1}0>$ basal texture (Fig. 2a, b and e) or a non-fiber feature (Fig. 2c and f) along the extrusion direction (For pure magnesium extruded at 100 °C, the overall texture is not typical of extruded magnesium alloys—the maximum intensity peak is offset from $<10\bar{1}0>$ by ~ 15°, contributed by unDRXed grains). The DRXed grains at two lower temperatures are responsible for the overall slightly weakened texture. The particle-induced fine grains in Mg–2Bi extruded at 300 °C do not substantially alter the texture character, with the intensity peak slightly tilted toward $<10\bar{1}0>$. In general, adding 2 wt% bismuth shows negligible influence on the recrystallized texture component and intensity in all the studied cases.

3.2.1 Grain Refining Mechanism in Mg–2Bi

We compare the morphology and distribution of Mg_3Bi_2 particles of Mg–2Bi extrudates to find out the reasons of formation of their distinct microstructure at different temperatures. SEM imaging in Fig. 3a and c show the microstructure of Mg–2Bi extruded at 100 °C and 300 °C. Mg_3Bi_2 constituent particles shown in Fig. 3a were deformed as thin strips up to ~ 200 μm long (maximum up to ~ 600 μm long) and were parallel with the extrusion direction. When extruded at higher temperatures, as shown in Fig. 3), Mg_3Bi_2 particles

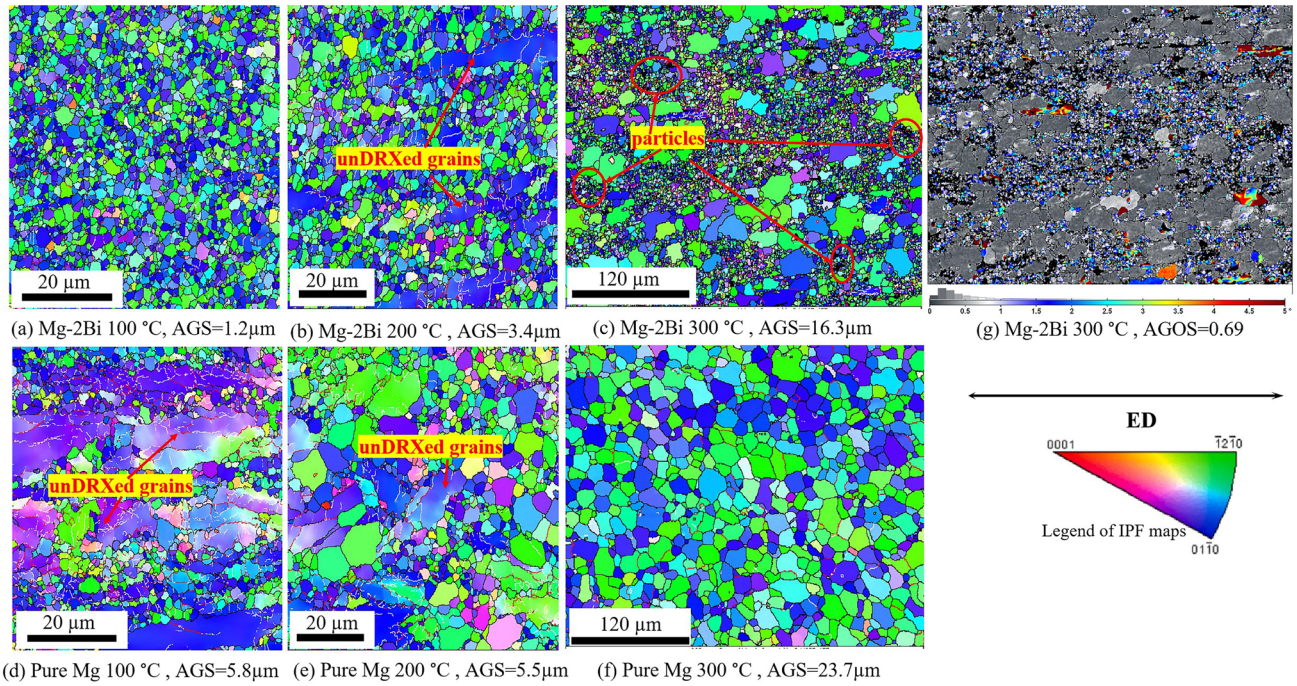

(a) Mg-2Bi 100 °C, AGS=1.2μm (b) Mg-2Bi 200 °C , AGS=3.4μm (c) Mg-2Bi 300 °C , AGS=16.3μm (g) Mg-2Bi 300 °C , AGOS=0.69

(d) Pure Mg 100 °C , AGS=5.8μm (e) Pure Mg 200 °C , AGS=5.5μm (f) Pure Mg 300 °C , AGS=23.7μm

(h)	100°C	200°C	300°C
Mg-2Bi Full texture	3.61 MUD	4.97 MUD	2.82 MUD
Mg-2Bi DRXed/PSN texture		3.1 MUD	3.07 MUD
Pure Mg Full texture	4.03 MUD	3.42 MUD	3.31 MUD
Pure Mg DRXed texture	3.11 MUD	3 MUD	

Fig. 2 EBSD inverse pole figure (IPF) colored maps for **a–c** Mg–2Bi and **d–f** pure magnesium extruded at different temperatures. White, red, and black lines in EBSD maps represent grain boundary angle 2°–5°, grain boundary angle 5°–10° and high angle grain boundaries > 10°, respectively. The average grain size (AGS) is labeled. The black irregulars highlighted with red circles in **c** are Mg_3Bi_2 particles. **g** shows the grain orientation spread (GOS) maps of the corresponding map of **c**. the average GOS is 0.69 with a standard deviation of 1.07. **h** are the corresponding micro-texture indicated by inverse pole figure, and X0 is the extrusion direction. MUD represents multiples of uniform distribution showing the maximum texture intensity

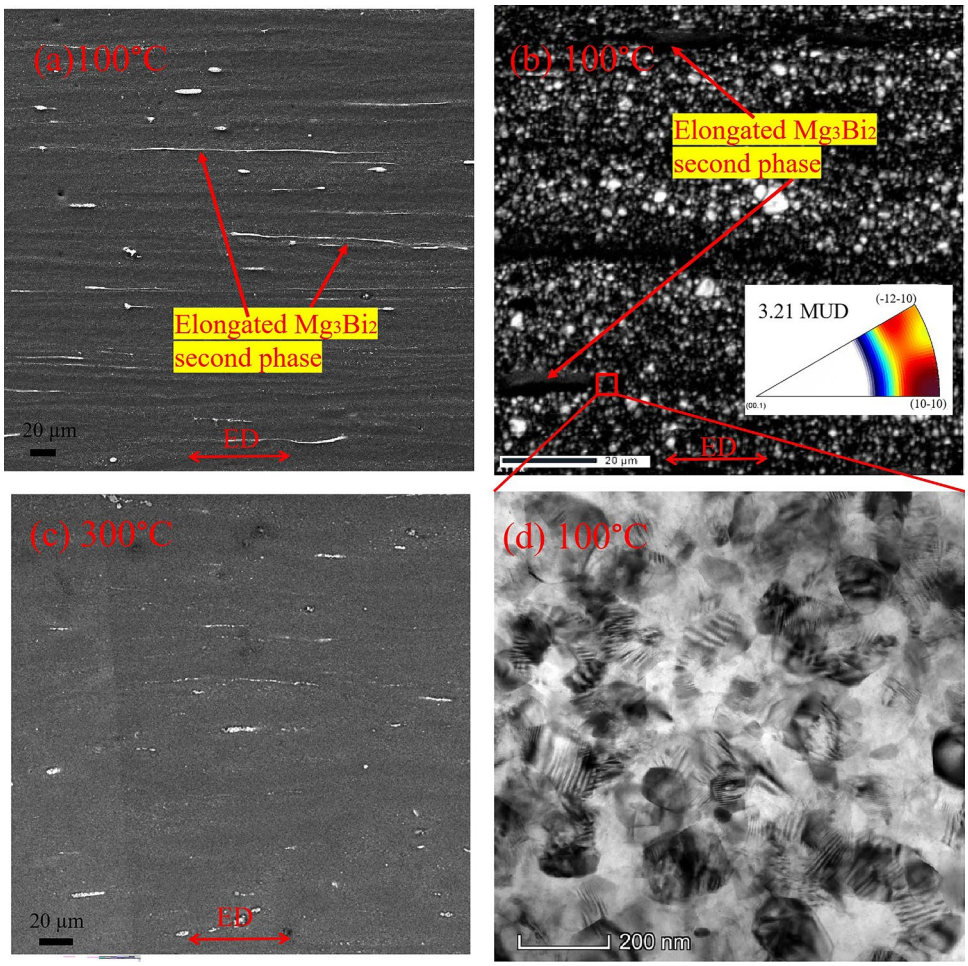

Fig. 3 SEM images of Mg–2Bi extruded at **a**100 °C and **c** 300 °C showing the morphology and spread of Mg_3Bi_2 particles. **b** EBSD band contrast map containing elongated Mg_3Bi_2 particles showing the grain structures in Mg–2Bi extruded at 100 °C and **d** is the microstructure of enlarged image of the red square at the tip of elongated Mg_3Bi_2 particles in **b** taken by TEM

break up into shorter rods or, in most cases, into irregular shapes, randomly distributed with the material flow. The shape and distributions of Mg_3Bi_2 constituent particles at 200 °C are in the middle of the above two states and not discussed here. An EBSD map containing elongated particles for material extruded at 100 °C is shown in Fig. 3b. Compared to the imaging area that avoided particles in Fig. 2a, the texture exhibits another peak (2.5 MUD) which is offset from $<11\bar{2}0>$ by ~ 13°, and the average grain size is even smaller, ~ 0.8μm. This is might due to the different magnitude of local lattice rotation and the strain mode from the particle-free domains [35]. We believe the fine grains in Mg–2Bi extruded at the two lowest temperatures are most induced by PSN. This PSN mechanism also contributes to the DRXed grains in Mg–2Bi when extruded at 300 °C, especially the fine grains in the bimodal grain microstructure.

The particle deformation zone around the particles [23, 36] (PDZ, as we analyzed by GOS in Fig. 2g, the area with high stored strain energy around the coarse particles) is the nucleation sites for PSN grains and affects the microstructure/texture. Sidor et al. [37] compared the PDZ generated by elongated and near equiaxed particles during rolling. They suggested the particles with a larger aspect ratio (length/width) induce higher strain gradient. The area fraction of PDZ (F_{PDZ} around a rod shaped particle can be expressed as [37]:

$$F_{PDZ} = f(\pi \frac{AB}{ab} - 1) \quad (1)$$

where f is the area fraction of particles (≈ 0.0133); A and B represent the length of ellipsoidal PDZ along and perpendicular to the particle strip, respectively; a and b are the length and thickness of particles, respectively. Although one cannot make an accurate assessment of the PDZ area induced by a single particle by the present data, the two cases can be roughly compared without considering the overlaps of PDZ simply by taking the total number (only the particle area > 3.14 μm^2 is counted.) of particles and average values of particle dimension in Fig. 3a and c, $a_{100°C}$ ~ 15 μm, $b_{100°C}$ ~ 2.4 μm, $a_{300°C}$ ~ 4.4 μm and $b_{300°C}$ ~ 2 μm. The total DRX area induced by PSN mechanism is crudely set as 100% for the case in Fig. 3a, and this value in Fig. 3c is assessed as ~ 55%, measured from Fig. 2c. So, the average

PDZ area for particles with a larger aspect ratio is estimated to be at least 8 times larger than that for smaller ones. Inspection of the EBSD band contrast map in Fig. 3b, the grains are not indexed at the tip band of the elongated particles. TEM shown in Fig. 3d reveals nano-sized grains in this area, with an average size of ~ 80 nm. Therefore, the lattice rotation at the tip band is extremely significant, promoting a high number density of PSN nuclei and resulting in a remarkable grain refining effect.

3.2.2 Strengthening Contributions from Grains

The effect of uniformly distributed grain size on the strengthening σ can be expressed by the Hall–Petch equation as follows [38, 39]:

$$\sigma = \sigma_0 + kd^{-1/2} \tag{2}$$

where σ_0 is the friction stress, d is the grain size, and k is the grain boundaries strengthening parameter. For the bimodal grain structure, the Hall–Petch relation is re-written as [40]:

$$\sigma = \left(\sigma_f + k_f d_f^{-\frac{1}{2}}\right) f_f + \left(\sigma_c + k_c d_c^{-\frac{1}{2}}\right) f_c \tag{3}$$

The subscript f denotes the fine grains and subscript c denotes the coarse grains. f_f and f_c are the volume fraction of fine grains and coarse grains, respectively. The value k depends on the deformation modes but is not impacted much by the alloying elements [41, 42]. In all the cases, the average Schmid factor of prismatic slip is in the range of 0.48–0.49 at the present loading conditions, hence the activation of prismatic slip determines the bulk yield stress. So k may not vary much. The micro-hardness of pure magnesium and the homogenized Mg–2Bi alloy after casting is ~ 25 HV and ~ 29 HV, respectively. So, the friction stress for Mg–2Bi employed in this work is ~ 1.2 times that of pure Mg. We set the grain size of 4.32 μm as the boundary of fine and coarse grains [43] for all the cases. The Hall–Petch parameters for fine and coarse grains of Mg–2Bi are σ_f = 80 MPa, k_f = 97 MPa·μm$^{1/2}$ and σ_c = 30 MPa, k_c = 260 MPa·μm$^{1/2}$ respectively [43]. The rough estimation for the increment of yielding stress of Mg–2Bi (compared to pure magnesium counterparts) due to the refined grain size $\Delta\sigma_{grainsize}$ is ~ 22 MPa, ~ 20 MPa, and ~ 23 MPa for extrusion temperatures of 100 °C, 200 °C, and 300 °C, respectively.

3.3 Dynamic Precipitation

3.3.1 Characterization of Dynamic Precipitation

Bright-field TEM images before and after the extrusion of Mg–2Bi alloys are shown in Fig. 4. In the homogenized sample of Fig. 4a, only a few Mg_3Bi_2 particles are observed. By contrast, a high population of particles can be observed in samples extruded at different temperatures. Two different morphologies including a sphere and a rod are clearly observed and un-uniformly distributed within grain interiors. It is found that most rod particles are not orientation related (as seen in Fig. 4d), thereby, they were probably those constituent particles that formed in casting, turning thickened in thermal mechanical process and deformed along the extrusion direction. The spherical particles, on the other hand, were dynamically precipitated during hot deformation, which were also observed by Jo et al. [21] in binary Mg–Bi alloys. The precipitates' size becomes larger with increasing the extrusion temperature, measured as ~ 21 ± 12 nm, ~ 41 ± 20 nm, and ~ 65 ± 31 nm, respectively. Arrays of the precipitates on the grain boundary can occasionally be observed in all alloys (red arrow indicated in (d)), which shows evidence of a Zenner pinning effect.

3.3.2 Strengthening Contributions of Dynamic Precipitates

Due to the interparticle spacing of rod-shaped particles is larger than 1μm, it is less likely that they could effectively strengthen the prismatic slip (the yielding of tensile testing at present cases is controlled by the prismatic slip [44]). The contributions of spherical nanoparticles to the strength increment $\Delta\tau$ on the prismatic plane can be expressed as [45]:

$$\Delta\tau = \frac{Gb}{2\pi\sqrt{1-v}\left(\frac{0.779}{f} - 0.785\right)d} \ln\frac{0.785d}{b} \tag{4}$$

where G is the shear modulus of magnesium (17 GPa), b is the magnitude of the Burgers vector (0.32 nm), v is the Poisson's ratio (0.3), and d is the average diameter. f is the volume fraction of precipitates, estimated as ~ 0.12%, 0.1%, and 0.1% with increases in the extrusion temperature (by TEM). The precipitates harden against the prismatic slip for ~ 8.9 MPa, ~ 5.4 MPa, and ~ 3.5 MPa as the extrusion temperature increases, respectively. Therefore, the yield stresses increment due to the dynamic precipitated Mg_3Bi_2 particles are estimated as ~ 17.8 MPa, ~ 10.8 MPa, and ~ 7 MPa (the maximum Schmid factor 0.5 is taken). Compared to the high number density precipitates generated by conventional static aging [44], dynamic precipitates in the present work are not an effective strength contributor.

3.4 Solute Clusters

3.4.1 Characterization of Bismuth Rich Clusters

In order to verify the possibility of the formation of Bi-clustering, high-angle annular dark-field scanning transmission electron microscopy (HAADF-STEM) was employed to

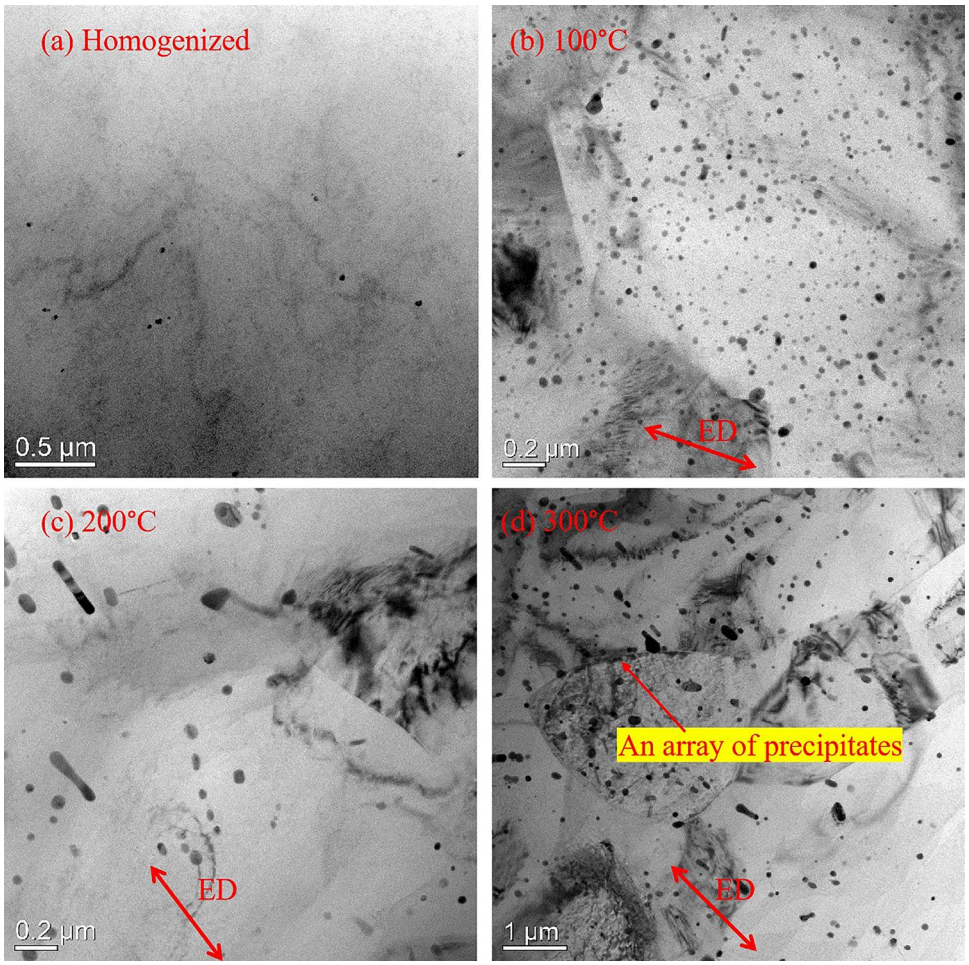

Fig. 4 The morphology of nanosized Mg_3Bi_2 particles taken by TEM for Mg–2Bi alloy **a** homogenized at 480 °C for 6 h and extruded at **b** 100 °C, **c** 200 °C, and **d** 300 °C

examine the microstructure at the atomic scale, as shown in Fig. 5. Bright zones with Z-contrast from Bi-rich clusters can be identified in all the cases. Bi clusters in the sample extruded at the lowest temperature are faint and sparsely distributed among the magnesium matrix. By contrast, the other two cases show a higher number density of the near-spherical and brighter contrast-featured clusters. The average diameter of the bismuth clusters in the two cases is similar. However, the number density per unit square micron increases to ~ 1.2 times for the sample extruded at 300 °C, compared with that extruded at 200 °C. This difference is mainly caused by accelerated diffusion kinetics from the improved vacancy concentration at higher deformation temperatures [46, 47]. First-principles studies have predicted a very large Bi-vacancy binding energy (0.14 eV) in magnesium among all the solutes indicating the greater possibility for forming Bi-clusters at higher temperatures. Moreover, solute clusters are prone to segregate along grain boundaries at higher extrusion temperatures as shown in Figs. 5d–f. The properties of the grain boundaries, dynamic recrystallization and deformation mechanisms may be influenced by the segregation of bismuth clusters, which will be investigated in future work.

3.4.2 Spatial Distributions of Bismuth Rich Clusters

Figure 6 displays the APT results for the alloys extruded at 200 °C. Figures 6a and b show the elemental distribution of magnesium and bismuth, respectively. A 0.74 at% Bi iso-concentration surface is used to delineate the bismuth solute clusters in Fig. 6c. Clearly, the distribution of bismuth is non-uniform. The concentration of bismuth in the dislocation core is significantly higher than that in the surrounding matrix. As shown in Fig. 6d, the corresponding proximity histogram is used to evaluate the average bismuth concentration around the dislocations, which is up to ~ 4.5 at% and an enrichment factor of 40 compared to the concentration of bismuth in solid solution. It is supposed that the dynamically diffusing bismuth atoms cluster in the region and segregate along the core of dislocations during hot extrusion (please see HAADF-STEM characterization of Bi atoms segregation to partial dislocations in reference [48]). A similar

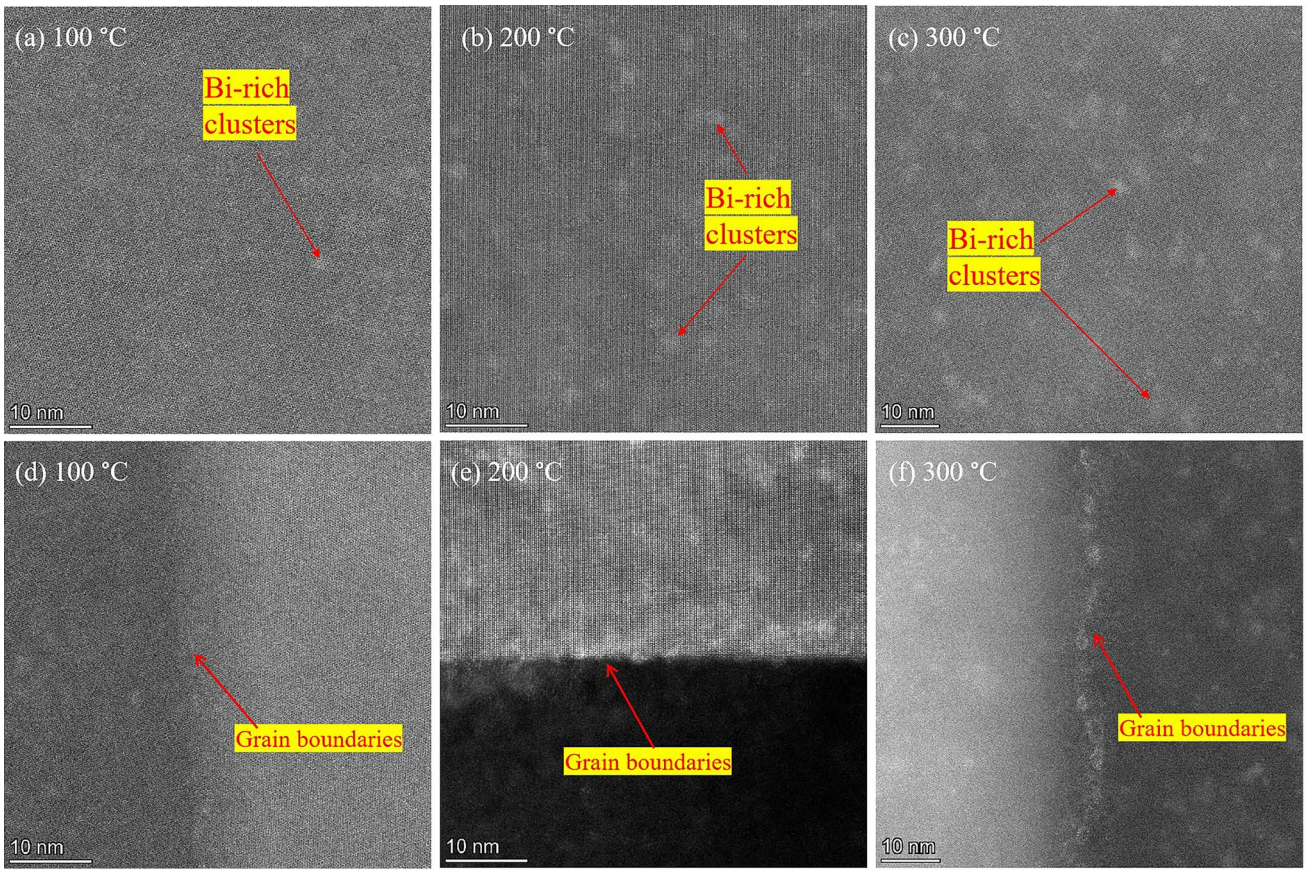

Fig. 5 HAADF-STEM images showing bismuth clusters in the magnesium matrix and the segregation at grain boundaries in Mg–2Bi extruded at **a d** 100 °C, **b e** 200 °C, and **c f** 300 °C

phenomenon was also reported by Bian et al. [28]. and Zeng et al. [27]. in dilute Mg–Al–Zn–Ca and Mg–Zn–Ca alloys. In their work, the co-clusters of Al–Ca–Zn or Ca–Zn are segregated to basal dislocations after 2% pre-strain and a short-time bake-hardening treatment, where a maximum of 25% increase in yield strength was attained.

3.4.3 Strengthening Contributions of Bismuth Clusters

The solute cluster hardening is believed to be caused by the cutting mechanism by dislocations, correlated to the cluster size, volume fraction, and physical properties, which can be expressed by Friedel's statistic shearing model [49]:

$$\Delta\sigma = k^{3/2} MG \sqrt{\frac{3}{2\pi b}} (f_v R)^{1/2} \tag{5}$$

where M is the Taylor factor (~2.5 for prismatic slip [50]), f_v is the volume fraction, which is estimated from APT as ~0.035% for alloys extruded at 200 °C, R is the radius of clusters (nm), and k is a constant related to the shearing mechanism (maximum value of ~0.1 is employed in this work [51]). Equation 5 predicts a strength contribution of ~27 MPa by bismuth clusters in Mg–2Bi extruded at 200 °C. If we take the volume fraction of bismuth cluster ~0.038% (~1.2 times that extruded at 200 °C estimated from Fig. 5) for Mg–2Bi extruded at 300 °C, the evaluated value slightly increases to ~29.5 MPa. For alloys extruded at 100 °C, solid solution strengthening, rather than cluster strengthening, plays a more important role due to the very low number density of bismuth clusters observed in this state.

The increment of the yielding strength of the present alloys can be described as:

$$\Delta\sigma = \Delta\sigma_{grainsize} + \Delta\sigma_{nanoparticles} + \Delta\sigma_{solidesolution} + \Delta\sigma_{clusters} \tag{6}$$

The net contribution from the solid solution can then be estimated by Eq. 6. The relative contributions of the hardening mechanism for alloys studied in the present work are summarized and shown in Table 1. It is clear that Hall–Petch hardening is always important for all the cases. Deformation-induced precipitation and solute clusters are

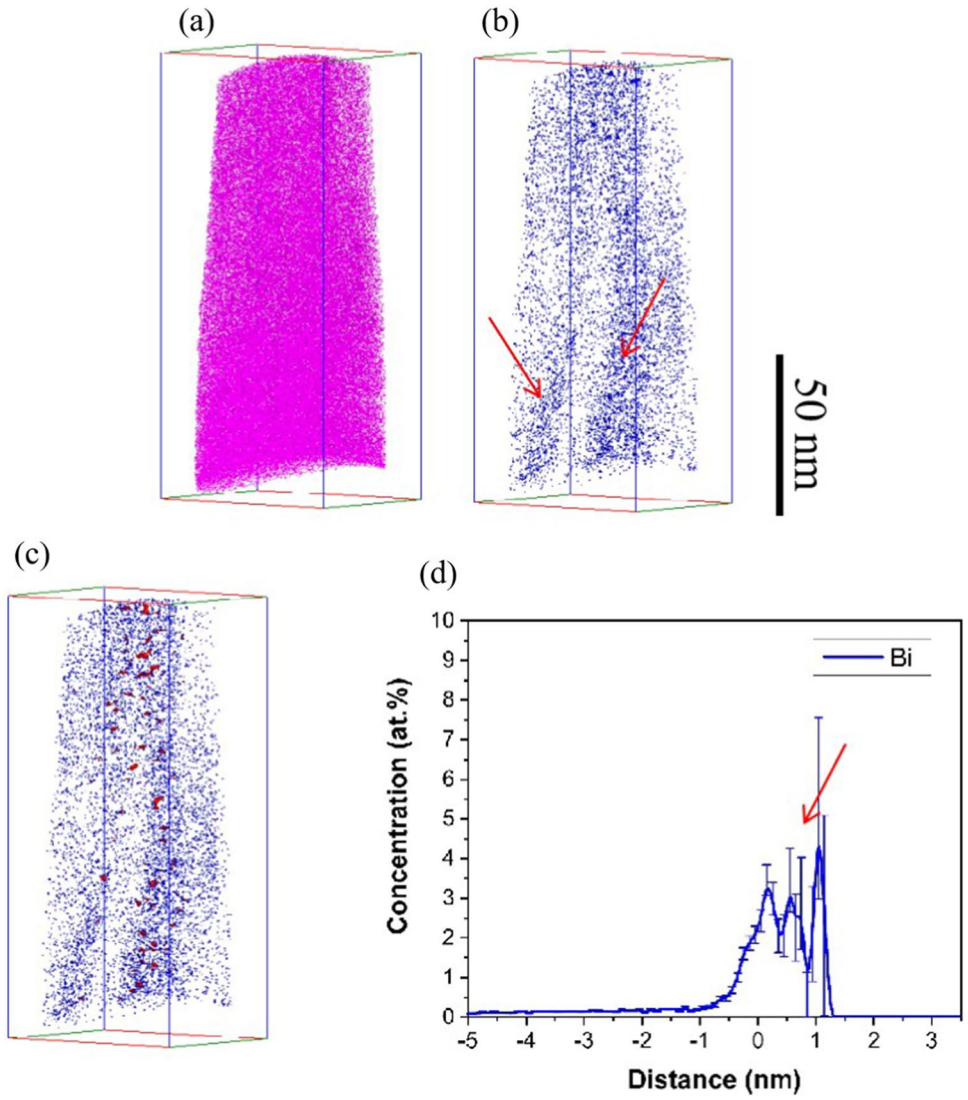

Fig. 6 Distribution of solute atoms of **a** magnesium (in purple) and **b** bismuth (in blue). The red arrows indicate the possible positions of the dislocation cores. **c** and **d** are the 0.74 at% iso-concentration surface of bismuth and the corresponding proximity histogram of bismuth, respectively

Table 1 Strengthening contributions from different strengthening mechanisms

	100 °C	200 °C	300 °C
$\Delta\sigma_{grainsize}$	~53%	~34%	~38%
$\Delta\sigma_{nanoparticles}$	~43%	~18%	~11%
$\Delta\sigma_{clusters}$	~4%	~46%	~50%
$\Delta\sigma_{solidesolution}$		~2%	~1%

responsible for the difference in yielding strength increment. Solute clusters in dilute magnesium alloys are demonstrated as an important hardening contributor. Therefore, our work provides the fundamental studies of dilute Mg–Bi binary alloy, so proper alloying and thermomechanical processing can be designed to manipulate the microstructure at multiscale to improve the mechanical properties further.

4 Conclusions

The current work has systematically investigated the effect of extrusion temperature on the mechanical responses and microstructure of dilute Mg–2Bi alloys at different scales. The main conclusions of the paper are the following:

1. Mg–2Bi alloy extruded at 100 °C showed the best mechanical properties with a yield strength of ~ 187 MPa and an elongation of ~ 25%. In contrast, the alloys extruded at higher temperatures show a decreasing yielding stress and ductility.
2. The addition of 2 wt% bismuth results in significant grain refinement at extrusion temperature lower than 200 °C. Particle stripes stimulated nucleation is the dominant mechanism for the observed ultra-fine grains. By contrast, the alloy extruded at 300 °C showed a bimodal grain structure. The constituent Mg_3Bi_2 phase

breaks up during extrusion, and the coarse fragments accelerate the local grain refinement. The particle deformation zone generated by Mg_3Bi_2 particles with a greater aspect ratio is larger than that of the near equiaxed particle size. The tip area of the particle stripe is shown to have a remarkable grain refining effect and it can refine the grain size down to ~ 80 nm (Fig. 3d).

3. All alloys are shown to have the typical basal texture, which is not weakened by the PSN effect.
4. The dynamic precipitation occurs during extrusion at all temperatures, with a particle size of ~ 21 nm, ~ 41 nm, and ~ 65 nm as the temperature increases. They provide the Zenner pinning effect to hinder grain growth.
5. Deformation-induced bismuth clusters are observed and characterized by HAADF-STEM and APT for the first time. Bismuth clusters are found to densely distribute in the matrix of two higher extrusion temperatures and segregate along the grain boundaries and the dislocations. The average size of clusters is similar in these two cases, but the distribution is slightly denser in the magnesium matrix of 300 °C.
6. In this work, the main contributors to the strength increment include PSN grains, deformation-induced nano precipitates, and bismuth clusters. Apart from the Hall–Petch hardening, the bismuth clusters also result in a more substantial hardening effect, accounting for half of the strengthening increment at two higher temperatures. Our findings are expected to provide new insights into manipulating the multiscale microstructure by new alloying and thermomechanical strategies to improve the synergy mechanical properties of dilute Mg–Bi-based alloys.

Acknowledgements This work is funded by the Yunnan Fundamental Research Projects (Grant No. 202201BE070001-038), Special Health Program of Zhejiang Province (Grant No. YS2022008) and Science and Technology Agency of Anhui Province (Project No. 202104a05020047 and No. 2022a05020032). The authors would like to acknowledge the support of the Deakin Advanced Characterization Facility.

Author contributions TG: Conceptualization, methodology, Investigation, Writing-original draft. YT: Preparation, Investigation, Writing-original draft. LJ: Preparation, Investigation, Formal analysis, Writing-review & editing. ZZ: Formal analysis. JW: Supervision, Formal analysis, Writing-review & editing.

Declarations

Conflict of interest The authors declare that they have no known competing financial interests or personal relationships that could have appeared to influence the work reported in this paper.

References

1. H. Wang, D.T. Zhang, C. Qiu, W.W. Zhang, D.L. Chen, Mater. Sci. Eng. A **851**, 143611 (2022)
2. H. Pan, G. Qin, Y. Huang, Y. Ren, X. Sha, X. Han, Z.-Q. Liu, C. Li, X. Wu, H. Chen, C. He, L. Chai, Y. Wang, J.-F. Nie, Acta Mater. **149**, 350–363 (2018)
3. T. Nakata, T. Mezaki, C. Xu, K. Oh-ishi, K. Shimizu, S. Hanaki, S. Kamado, J. Alloy. Compd. **648**, 428–437 (2015)
4. W. Cheng, Y. Liu, Y. Zhang, S. Meng, S. Arthanari, H.-X. Wang, L. Wang, Met. Mater. Int. **27**, 4510–4516 (2021)
5. Q. Wang, H. Zhai, L. Wang, J. Xu, Y. Chen, B. Jiang, Mater. Sci. Eng. A **860**, 144309 (2022)
6. Q. Wang, H. Zhai, L. Liu, Z. Jin, L. Zhao, J. He, B. Jiang, J. Alloy. Compd. **924**, 166337 (2022)
7. Q. Wang, H. Zhai, L. Liu, H. Xia, B. Jiang, J. Zhao, D. Chen, F. Pan, J. Magnes. Alloys **10**, 2588–2606 (2022)
8. H. Yu, Y. Liu, Y. Liu, D. Wang, Y. Xu, B. Jiang, W. Cheng, W. Tang, F. Yin, W. Yu, J. Market. Res. **24**, 940–951 (2023)
9. Y.-Q. Zhang, W.-L. Cheng, H. Yu, H.-X. Wang, X.-F. Niu, L.-F. Wang, H. Li, J. Mater. Sci. Technol. **105**, 274–285 (2022)
10. G.-L. Liu, W.-L. Cheng, L. Luo, H. Yu, L.-F. Wang, H. Li, H.-X. Wang, J.-H. Wang, J. Market. Res. **25**, 497–510 (2023)
11. S.J. Meng, H. Yu, S.D. Fan, Y.M. Kim, S.H. Park, W.M. Zhao, B.S. You, K.S. Shin, Mater. Lett. **261**, 127066 (2020)
12. Y.-H. Liu, W.-L. Cheng, Y. Zhang, X.-F. Niu, H.-X. Wang, L.-F. Wang, J. Alloy. Compd. **815**, 152414 (2020)
13. F. Kong, H. Feng, H. Chen, Y. Lin, Y. Wang, W. Xie, G. Wei, Y. Yang, X. Peng, Met. Mater. Int. (2023). https://doi.org/10.1007/s12540-023-01516-5
14. K. Huang, R. E. Logé, Zener Pinning, in *Reference Module in Materials Science and Materials Engineering*, ed. by H. Saleem (Elsevier, Amsterdam, 2016)
15. T.T. Sasaki, T. Ohkubo, K. Hono, Scripta Mater. **61**, 72–75 (2009)
16. C. He, C.Q. Liu, H.W. Chen, J.F. Nie, J. Alloy. Compd. **815**, 152419 (2020)
17. M.R. Barnett, A. Sullivan, N. Stanford, N. Ross, A. Beer, Scripta Mater. **63**, 721–724 (2010)
18. L.W.F. Mackenzie, M.O. Pekguleryuz, Scripta Mater. **59**, 665–668 (2008)
19. N. Stanford, Mater. Sci. Eng. A **527**, 2669–2677 (2010)
20. S. Meng, H. Yu, L. Li, J. Qin, S.K. Woo, Y. Go, Y.M. Kim, S.H. Park, W. Zhao, F. Yin, B.S. You, K.S. Shin, J. Alloy. Compd. **834**, 155216 (2020)
21. J. Go, J.U. Lee, H. Yu, S.H. Park, J. Mater. Sci. Technol. **44**, 62–75 (2020)
22. T. Guo, X. Lu, R.K. Varma, C. Zhao, J. Wang, J. You, J. Chen, Front. Mater. (2021). https://doi.org/10.3389/fmats.2021.633789
23. J. Humphreys, G.S. Rohrer, A. Rollett, in *Recrystallization and Related Annealing Phenomena*, 3rd edn. (Elsevier, Amsterdam, 2017), pp. 321–359
24. T. Guo, S. Babaniaris, J. Wang, Q. Chao, J. Mater. Sci. **57**, 21537–21551 (2022)
25. V.M. Miller, T.M. Pollock, Metall. Mater. Trans. A **47**, 1854–1864 (2016)
26. H. Somekawa, A. Singh, Scripta Mater. **150**, 26–30 (2018)
27. Z.R. Zeng, Y.M. Zhu, M.Z. Bian, S.W. Xu, C.H.J. Davies, N. Birbilis, J.F. Nie, Scripta Mater. **107**, 127–130 (2015)
28. M.Z. Bian, T.T. Sasaki, T. Nakata, Y. Yoshida, N. Kawabe, S. Kamado, K. Hono, Acta Mater. **158**, 278–288 (2018)
29. M. Murayama, K. Hono, Acta Mater. **47**, 1537–1548 (1999)
30. E.V. Pereloma, A. Shekhter, M.K. Miller, S.P. Ringer, Acta Mater. **52**, 5589–5602 (2004)

31. T.T. Sasaki, J.Y. Lin, P. Yi, Z.H. Li, S.E. Prameela, A. Park, E. Lipkin, A. Lee, M.L. Falk, T.P. Weihs, K. Hono, Scripta Mater. **220**, 114924 (2022)
32. H. Somekawa, A. Singh, R. Sahara, T. Inoue, Sci. Rep. **8**, 656 (2018)
33. G. Liu, J. Zhang, Y. Dou, Comput. Mater. Sci. **103**, 97–104 (2015)
34. Z. Zeng, N. Stanford, C.H.J. Davies, J.-F. Nie, N. Birbilis, Int. Mater. Rev. **64**, 27–62 (2019)
35. F. Dunne, R. Kiwanuka, A. Wilkinson, Proceedings of the royal society A: mathematical. Phys. Eng. Sci. **468**, 2509–2531 (2012)
36. F.J. Humphreys, Scripta Mater. **43**, 591–596 (2000)
37. J.J. Sidor, K. Decroos, R.H. Petrov, L.A.I. Kestens, Int. J. Plast. **66**, 119–137 (2015)
38. E.O. Hall, Proc. Phys. Soc. Sect. B **64**, 747–753 (1951)
39. D. Gu, J. Peng, J. Wang, F. Pan, Met. Mater. Int. **27**, 1483–1492 (2021)
40. Z.-Z. Jin, M. Zha, Z.-Y. Yu, P.-K. Ma, Y.-K. Li, J.-M. Liu, H.-L. Jia, H.-Y. Wang, J. Alloy. Compd. **833**, 155004 (2020)
41. H. Yu, C. Li, Y. Xin, A. Chapuis, X. Huang, Q. Liu, Acta Mater. **128**, 313–326 (2017)
42. B.Q. Shi, Y.Q. Cheng, X.L. Shang, H. Yan, R.S. Chen, W. Ke, Mater. Sci. Eng. A **743**, 558–566 (2019)
43. R. Zheng, J.-P. Du, S. Gao, H. Somekawa, S. Ogata, N. Tsuji, Acta Mater. **198**, 35–46 (2020)
44. J. Jain, P. Cizek, W.J. Poole, M.R. Barnett, Acta Mater. **61**, 4091–4102 (2013)
45. J.F. Nie, Scripta Mater. **48**, 1009–1015 (2003)
46. W.T. Sun, X.G. Qiao, M.Y. Zheng, C. Xu, S. Kamado, X.J. Zhao, H.W. Chen, N. Gao, M.J. Starink, Acta Mater. **151**, 260–270 (2018)
47. W. Sun, Y. Zhu, R. Marceau, L. Wang, Q. Zhang, X. Gao, C. Hutchinson, Science **363**, 972–975 (2019)
48. C. He, Y. Zhang, Z. Li, H. Chen, J.-F. Nie, J. Magnes. Alloys (2022). https://doi.org/10.1016/j.jma.2022.11.021
49. A. Deschamps, Y. Brechet, Acta Mater. **47**, 293–305 (1998)
50. C.H. Caceres, P. Lukac, Phil. Mag. **88**, 977–989 (2008)
51. L. Jiang, R.K.W. Marceau, B. Guan, T. Dorin, K. Wood, P.D. Hodgson, N. Stanford, Materialia **8**, 100462 (2019)